

Magnetic Sensors on Flexible Substrates

Ana Catarina Janeiro
ana.janeiro@tecnico.ulisboa.pt

Instituto Superior Técnico, Universidade de Lisboa, Portugal

November 2019

Abstract

Magneto-resistive sensors have attracted much interest in the past decades due to their high sensitivity, low cost and power consumption and small size. In order to achieve the same functionality on flexible substrates as on rigid, the magnetoelastic properties of thin films and deformability of polymers must be understood in depth. In this work we study the optimization of the microfabrication process of anisotropic magneto-resistive sensors on flexible substrates. Two different polymers were used, namely Polyimide (25 and 125 μm) and Polyethylene naphthalate and also two ferromagnetic alloys were deposited as thin films. The as-deposited materials are studied for their crystalline and magnetic properties, using X-ray diffraction and Vibrating Sample Magnetometer techniques. The structures design has been optimized throughout the fabrication, as obstacles appear, and SEM imaging is used to identify defects in the fabricated structures. Five samples were successfully fabricated and their magneto-transport properties were measured through a custom bending setup integrated on the existing apparatus at INESC-MN. A maximum AMR ratio of 0.90% was accomplished, which is very close to silicon counterparts. PI-125 μm seems to be the best substrate for the sensor layer, as it yielded better AMR signal, it has the drawback of not reaching the same curvature as easily as PEN-75 μm and PI-25 μm . The thinner polyimide shows the lowest AMR ratio, but on the other hand it also presents the lowest saturation field and stress values, with the advantage of conforming to almost any shape.

Keywords: Anisotropy, Magneto-resistance, Flexible substrate, Magnetostriction, Induced stress

1. Introduction

Magneto-resistive sensors have attracted much interest in the past decades due to their high sensitivity, low cost and power consumption and small size [1, 2]. While silicon has been the most used substrate for device fabrication, due to its useful properties as a semiconductor material, the novel applications of portable and wearable electronics have been driving a push towards materials with higher mechanical flexibility and compactness [3]. For instance, monitoring the temperature of the human body is an example of an important parameter in physiology that needs attention in terms of finding novel sensors that can be integrated with soft, flexible and curvilinear matter [4]. To this end, several research groups have been focusing on reaching the same levels of performance and sensitivity on flexible substrates as the existing on rigid counterparts.

Anisotropic magneto-resistance was the first magneto-resistive effect to be observed and implemented at industrial scale, although it was rapidly substituted by Giant magneto-resistance due to its higher MR ratio. However, this technology presents drawbacks relatively to AMR, since there is a need for

external magnetic bias, increasing the volume and power consumption of the final product. Furthermore, the GMR response is not practical at low magnetic fields, yielding a small resistance change. On the contrary, AMR sensors are self-biased and can alleviate this disadvantage presenting higher sensitivities at smaller fields [5].

2. Background

2.1. Magnetic anisotropy and Magneto-resistance

On the atomic level, different sources that cause magnetic anisotropy can be identified. The spontaneous magnetization of the domains tends to lie along one or more easy directions determined by crystal structure, atomic-scale texture or sample shape. This tendency is represented by the anisotropy energy E_a , in which the leading term is:

$$E_a = K_u \sin^2 \theta \quad (1)$$

where θ is the angle between magnetization and the anisotropy axis and K_u is the anisotropy constant, with units of J m^{-3} . These values can range from less than 1 kJ m^{-3} to more than 10 MJ m^{-3} .

The anisotropy field, H_a is derived minimizing the energy term, and is defined as the field needed to saturate the magnetization of a uniaxial crystal in a hard direction:

$$H_a = \frac{2K_u}{\mu_0 M_s} \quad (2)$$

Since $\mu_0 M_s \sim 1$ T for a typical ferromagnet, H_a values are of the order of 2.5 mT to more than 32 mT [6].

There are essentially three causes of anisotropy in a material: shape, magnetocrystalline and induced anisotropy.

2.2. Magnetostriction

Magnetostriction can be generally described as the change in size of a material due to its magnetization process. This change can be either in volume, which in this case is isotropic and reflects a change in interatomic spacing, or linear in the direction of magnetization.

In general, if θ is the angle between the magnetization and the easy axis:

$$\lambda(\sigma) = \frac{\lambda_s(3 \cos^2 \theta - 1)}{2} \quad (3)$$

Linear strain changes are related to the rotation of domains as the magnetization saturates. Two distinct effects fall in this category, namely the Joule and Villari effect. James Joule observed in 1842 the change in size of a nickel rod during a magnetization process.

The Villari effect (also known as inverse magnetostriction) happens when mechanical stress is applied to a demagnetized sample, modifying its easy axes for magnetization, which will be the focus of this work.

2.3. Anisotropic Magnetoresistance

The AMR effect was discovered in 1857 by William Thompson, by observing that the resistivity of Ni varies slightly with the direction of current, relative to the direction of magnetization [7]. This mechanism occurs in 3d transition metals and is due to spin-orbit coupling, demonstrating the interaction between the spin of the conduction electrons and the crystal lattice. An increase in the resistivity of the system occurs as the majority s-electrons are scattered into (minority) d-orbital states. This anisotropic scattering has a probability of occurring that depends on the orientation of magnetization relative to the flowing current. If the d-orbitals are parallel to the current direction, the resistivity is higher, whereas if they are perpendicular, it will be lower [8]. As depicted in Fig.??, the change in resistivity depends on θ , the angle between the direction of the current and magnetization. Eq.4 describes

this phenomenon, where ρ_{\perp} and ρ_{\parallel} refer to the resistivity values at $\theta = 90^\circ$ and $\theta = 0^\circ$, respectively [9].

$$\rho(\theta) = \rho_{\perp} + (\rho_{\parallel} - \rho_{\perp}) \cos^2 \theta \quad (4)$$

Typical AMR values at room temperature are $\sim 5\%$ for NiFe and CoFe bulk alloys [9] and lower for patterned thin films ($\sim 2\%$) [10]. This reduction is caused by additional scattering, for example at grain boundaries and film interfaces.

3. State of the art

AMR sensors started to gain popularity around the 1980's as high density read heads for tape and disk drives [2], but these were rapidly substituted by GMR technology, as the latter yields higher MR ratios. Other common applications include automotive wheel speed and crankshaft sensing, compass navigation, vehicle detection, current sensing, and many others [11].

Practically all AMR devices assume a “barber pole” structure composed of aluminum stripes sputtered on permalloy (Py) strips that deflect the direction of the current by 45° with respect to the direction of magnetization, so that the change in resistance is linear and the largest. Four of these elements are connected in a Wheatstone bridge (Fig. 1), in which the sensitivity of two branches have the opposite direction than the other two, in order to double the signal output.

They are often composed of a single layer of Permalloy ($\text{Ni}_{80}\text{Fe}_{20}$) thin film designed in a meander shape to induce a strong anisotropy and maximize the length of the sensing element.

Although the bridge configuration is the most common, there are other types of AMR sensors, which was the case in the work of Ger et al., that fabricated a rolled-up structure with a layer of Permalloy in silicon substrate for cell sensing. The cells were labeled with magnetic nanoparticles, which in turn were attracted towards the sensors and MR measurements were performed. This 3D biosensor has the potential to integrate microfluidic channels for cell detection and counting with high accuracy which is important for health monitoring and diagnosis applications [12].

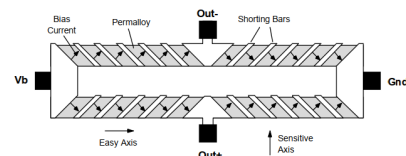


Figure 1: AMR sensor barber pole configuration. (Reused from [?] © Honeywell, Inc).

When it comes to device fabrication, flexible polymers can offer lower costs when compared to silicon, less fabrication steps and feature high mechanical flexibility [13].

Wang et al. successfully fabricated self-biased AMR magnetic field sensors with a sensitivity limit around 1.5×10^{-3} Oe at 3 Hz and a sensitivity of 42 T^{-1} , close to the value on rigid Si substrate and superior to GMR counterparts [5].

GMR sensors came along after AMR, demonstrating higher magnetoresistance ratios between 10% to 80%. This effect occurs in a multilayer sandwich of two magnetic layers that are separated by a thin non-magnetic film [13]. Based on the inverse magnetostriction effect of magnetic layers, Kwon et al. fabricated spin-valve structures of Ta/NiFe/CoFe/Cu/Ni/IrMn/Ta on PI substrate (125 μm). The MR ratio of 2.3% measured in the initial flat state gradually increases to 7.0% in the after flat state for 100-times bending due to the enhanced magnetic anisotropy of the pinned layer in spite of the reduction of the anisotropy in the free layer [14].

4. Thin film characterization

Thin films of $\text{Ni}_{80}\text{Fe}_{20}$ and $\text{Co}_{90}\text{Fe}_{10}$ were deposited on the N3000 and N2000 systems, respectively, with a nominal thickness of 200 \AA , and encapsulated with 100 \AA of Ta on top of Polyimide and PEN substrates. The resistivity measurements, X-ray diffraction and Vibrating sample magnetometer analysis were performed on these materials.

4.1. Resistivity

Firstly, the resistance of thin metallic films grown on glass and polymer (calibration samples) was measured with the four-probes method. For this purpose, a simple system built at INESC-MN with 4 probes equally spaced was connected to a Keithley 2000 multimeter with 4 wire sensing mode, and current was swiped from -5 mA to 5 mA in steps of 1 mA. Electric current is applied through the outer probes, while voltage is measured across the inner probes, diminishing contact resistance and increasing the accuracy of the measurements.

Assuming an uniform cross section, the resistivity is given by:

$$\rho = R \frac{A}{l} \quad (5)$$

where R is the resistance, $A = w \times t$ is the area of the cross-section and l, w, t are the length, width and thickness of the material, respectively. The SI units for this quantity are $\Omega\cdot\text{m}$.

The resistivity value obtained for the $\text{Ni}_{80}\text{Fe}_{20}$ film on glass is in accordance with results previously observed at INESC using the same deposition

technique [8]. As for the resistivities on flexible substrates, these samples have a layer of 200 \AA in comparison with the 500 \AA on glass, which results in an increase in the resistivity value. Moreover, these substrates have a higher surface roughness than the conventional rigid substrates, leading to films with smaller grain sizes. This implicates more roughness at interfaces, promoting scattering and diffusion at grain boundaries, thus increasing resistivity [15].

$\text{Co}_{90}\text{Fe}_{10}$ resistivity values are in accordance with [10]. In addition, this material also exhibits an increase in resistivity when deposited on flexible substrates.

4.2. X-ray diffraction (XRD)

In order to better understand the influence of these flexible substrates on film growth, x-ray diffraction was used on samples both with $\text{Ni}_{80}\text{Fe}_{20}$ and $\text{Co}_{90}\text{Fe}_{10}$ with a layer of 500 \AA (with bottom and top Ta). A total of 9 samples were measured, corresponding to the substrates alone and two films in the three substrates. The equipment is controlled by a computer software where one inserts the desired parameters, namely the 2θ range (5 - 50 in this case), step and acquisition time per step.

From the peak positions $2\theta_0$, the distance between adjacent atom planes d_{exp} was calculated using Bragg's law.

The results showed that the polyimide substrates are amorphous, as expected, and PEN presents a sharp peak at $2\theta \approx 12^\circ$. This is probably due to its fabrication process, which causes its partial crystallization, as stated on the datasheet. The calculated interplanar distance is 3.40 \AA , which is very close to the result seen in literature: 3.33 \AA . This peak corresponds to the (-1 1 0) plane in the crystal form α , which is known to be orthorhombic.

In the case of $\text{Ni}_{80}\text{Fe}_{20}$, for all three substrates, a peak appears at $2\theta \approx 20^\circ$. According to literature, this is a highly crystalline peak related to the (1 1 1) orientation in face-centered cubic (FCC) structures [16]. Two weaker peaks should also appear, corresponding to orientations (2 0 0) and (2 2 0), but that was not the case in this work, probably due to the high degree of texture of the deposited thin films, which exhibit a strongly preferred orientation.

The results yielded the same interplanar distance for all three samples, which is a good indicator that the film is growing in the same structure on the different substrates. In addition, the obtained value for this property is in accordance to d_{teor} [17].

$\text{Co}_{90}\text{Fe}_{10}$ samples did not yield meaningful results, but it is known from literature that its structure is BCC, normally exhibiting the (110) and (200) peaks.

4.3. Vibrating sample magnetometer (VSM)

A study of the magnetic properties of the samples was performed prior to fabrication, for validation of the sensors characterization results, and also as another test to the thin films quality. For such, a vibrating sample magnetometer (DMS 1660 system) was used to acquire a hysteresis loop for each sample.

The samples were measured in two directions, the easy axis (induced by a magnetic field during film deposition) and the hard axis, orthogonal to the first. A magnetic field from -100 mT to 100 mT was applied during all measurements. We can extract valuable information from both curves, namely the coercive (H_c) field from the first and anisotropy (H_k) field and saturation magnetization (M_s) from the latter.

According to the Stoner-Wohlfarth model [6], when the field is applied in the direction of the easy anisotropy axis, the coercivity is equal to the anisotropy field:

$$H_c = \frac{2K_u}{\mu_0 M_s} \quad (6)$$

where K_u is the sum of the magnetocrystalline and shape anisotropy [6].

$\text{Co}_{90}\text{Fe}_{10}$ results present a higher coercivity and anisotropy field than $\text{Ni}_{80}\text{Fe}_{20}$, as expected, since it has a much higher contribution from the magnetocrystalline anisotropy. Furthermore, the coercive field values are in accordance to literature [18].

$\text{Ni}_{80}\text{Fe}_{20}$ coercivity values are also as expected, it has a low coercive and anisotropy field due to its low magnetostriction [19]. Values for the anisotropy field are in accordance with [20], [21] and as for the coercive field, very similar results were obtained on Kapton HN [22].

As for the substrate influence, it appears to be almost negligible. When looking at both $\text{Ni}_{80}\text{Fe}_{20}$ and $\text{Co}_{90}\text{Fe}_{10}$ few differences can be observed, as all values are of the same order. However, there seems to be a slightly influence on $\text{Co}_{90}\text{Fe}_{10}$, as there is a bigger dispersion of the H_c and H_k values.

From H_k results, the effective anisotropy constant was estimated through the following equation:

$$K_u = \frac{H_k \mu_0 M_s}{2} \quad (7)$$

with $\mu_0 = 4\pi \times 10^{-7} \text{ J/A}^2/\text{m}$ and theoretical M_s values of 830 kA/m [6] and 1600 kA/m [?] for $\text{Ni}_{80}\text{Fe}_{20}$ and $\text{Co}_{90}\text{Fe}_{10}$, respectively. These values represent a rough but valid estimate for the anisotropy, with $\text{Co}_{90}\text{Fe}_{10}$ values with one order of magnitude bigger than $\text{Ni}_{80}\text{Fe}_{20}$.

5. Fabrication process

5.1. Overview

A general overlook of the process is illustrated in fig. 2 and each step designation is described below.

(a) Stack deposition; (b) 1st level of lithography to design and protect the sensor (inverted mask); (c) Etching and photoresist strip; (d) 2nd level of lithography to define the electrical contacts (non-inverted mask); (e) Deposition of electrical contacts (AlSiCu or Au); (f) Lift-off to remove the photoresist.

5.2. 1st lithography: sensor layer

After material deposition, the next task is to define the sensors. This operation consists of defining the sensor shape, and is accomplished by a direct-write laser (Heidelberg DWL 2.0) that exposes a photo-sensitive polymer (photoresist) through the desired mask, to be revealed after development. To define which areas are to be exposed, a mask file is created in AutoCAD software, and subsequently converted and divided into 200 μm wide stripes, which are exposed in sequence. A two layer mask was created in AutoCAD and was continuously altered throughout the fabrication of several samples.

The first layer is inverted, and it is the one that underwent more changes. The substrate size was 1 \times 2 inches, and the mask die was 19000 \times 35000 μm . The first version of the mask served as test, only one sensor was designed and the five pairs of contacts were all redundantly connected to the sensor. It had a projected nominal resistance of 1k Ω so we could have a fairly good electrical output. Each stripe is 150 \times 15000 μm . The next two versions of the mask had five sensors plus several others for testing.

5.3. Etching by ion-beam

The etching step was performed in Nordiko 3000, the same machine used for $\text{Ni}_{80}\text{Fe}_{20}$ deposition that was described in the previous chapter. This step is made in order to remove all the material from the sample, except the sensor stripes protected with photoresist. The etching is only supposed to stop when the substrate is reached. Since all samples had 400 \AA of material, in the first samples fabricated, the programmed etching times were 400 seconds. This rate worked for $\text{Ni}_{80}\text{Fe}_{20}$, but it wasn't

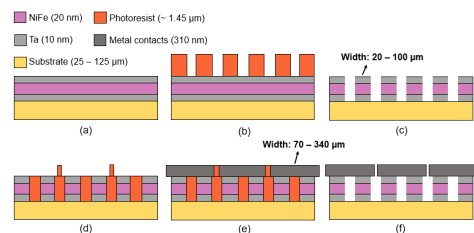


Figure 2: Fabrication process overview.

enough to remove all the material from $\text{Co}_{90}\text{Fe}_{10}$ samples. This is due to this material being harder than $\text{Ni}_{80}\text{Fe}_{20}$, so the etching time had to be prolonged for 500 or even 600 seconds in some cases. To assure that the etching step is completed, a multimeter is used in the substrate area to test for any electrical contact, since the polymers are not conductive, there should be no electrical output.

5.4. Photoresist strip

The etching step should be immediately followed by the photoresist strip, as the longer it stays on the sample, the more it hardens and becomes difficult to dissolve and remove. In order to do so, the sample is placed in a glass beaker and submerged in acetone for about 5 minutes. To help dissolve the PR faster, the container was manually agitated or placed in the ultrasounds for 2 to 3 minutes. When it seems that all PR has dissolved from the sample surface, the sample is rinsed with IPA (isopropyl alcohol) and deionized water. Once again, the sample is observed with the help of the optical microscope to check if in fact all the PR has disappeared.

Sometimes incomplete striping of the PR happens. When this occurs, the sample needs to return to acetone a few more minutes.

5.5. 2nd lithography: electrical contacts

The second level of lithography is a non-inverted mask that defines the metal pads and leads that make the connections between sensors and the characterization acquisition system. The coating process was very similar to the first, but with the detail of making a pre-development (20 seconds) of the PR right after coating and prior to the lithography. This is mostly done in non-inverted layers that will further undergo a lift-off step, to improve the photoresist profile and facilitate its removal. Furthermore, when exposing a layer for lift-off, the amount of energy used is usually increased, and in this particular case it was 95% of 100 mW (maximum laser output power).

After lithography and development, the PR covers all the sample surface, except for the spots designed on the exposure where the photoresist dissolved. These spots will then be filled with metal

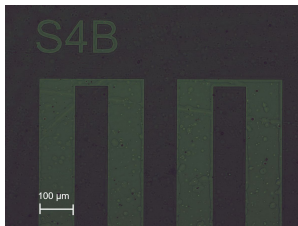


Figure 3: Optical microscope image of $\text{Ni}_{80}\text{Fe}_{20}$ sample after etching.

to achieve electric contact. An example of a sensor after the second exposure is shown in Fig.4.

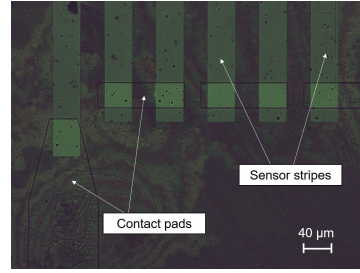


Figure 4: Example of sensor S2 after the second lithography.

5.6. Metallization and lift-off

To establish the electric contacts, a layer of metal (namely $\text{Al}_{98.5}\text{Si}_1\text{Cu}_{0.5}$) is deposited in Nordiko 7000, a multi-process system that features 4 chambers plus a dealer chamber. To perform this task only 3 of the 4 modules are used: module 2 does a sputter etch with Ar ions, which is used for a 30-60 seconds soft etch to clean the sample surface prior to metallization; Modules 4 is for depositing the $\text{Al}_{98.5}\text{Si}_1\text{Cu}_{0.5}$, which in this case was 3000 Å and module 3 was used for 100 Å TiW deposition that protects the contacts from oxidation. The depositions in N7000 are achieved through DC magnetron sputtering.

The power applied to the target during deposition is usually 0.5 kW but it had be decreased to 0.25 kW so the substrate doesn't suffer great temperature variations. In addition, the deposition of AlSiCu was made in a total of 6×500 Å steps with 5 cool down steps of 300 seconds between each deposition.

Alternatively to N7000, in the last batch of samples the metallization step was made in a different machine.

The metal available in this machine for depositing contacts is gold, with a buffer layer of chromium to improve adhesion. For this purpose, 100 Å Cr + 1000 Å Au were deposited. In fig. 5 samples after deposition in Alcatel are shown still in the proper machine holder.

5.7. Lift-off

Lift-off is the last step of this process, and most times one of the most critical. When fabricating on rigid substrates, a commonly used reagent is Microstrip (as well as for PR strip) but as it requires a 65 °C bath, it's not recommend for polymers. Instead, acetone is used once more to remove the photoresist and the excess metal on top. This step is very similar to the striping of photoresist after etch, but sometimes takes a little more time to remove everything. There's also an additional challenge with the 25 µm polyimide, as it rolls itself inwards when

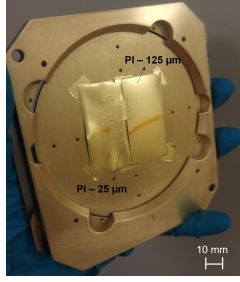


Figure 5: Samples after gold contacts deposition in Alcatel; Left sample is PI-25 substrate and right one is PI-125.

submerged in acetone for a couple of minutes, as it's shown in fig. 6. In this case, the lift-off is interrupted, the sample is cleaned with IPA and DI water to make it flat again, and then the process restarts. On average, the samples took 6 to 7 minutes to remove all the metal and photoresist, always with the help of ultrasounds.

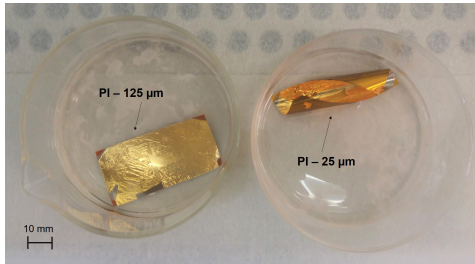


Figure 6: Samples with gold metallization from Alcatel in lift-off process; Sample on the left is PI-125 and on the right is PI-25.

5.8. Fabrication challenges and mitigation

Fabricating on flexible substrates is a challenge, as the established techniques for silicon and glass are not the most indicated and need adaptations. In addition to changes already described above, such as using acetone to dissolve the PR instead of microstrip or a different holder during lithography, there were more technicalities that will be explained in this section.

The first obstacle appeared on the coating step of the samples. When performing the lithography of the first sample, film cracks were visible in the laser camera. After the lithography process, the sample was inspected in the optical microscope and the defects were visible (Fig. 7). The fabrication of the sample proceeded and when trying to measure the magnetic transport we came to the conclusion that it was open circuited. After some tests it was seen that in fact, if the cracks cross the majority of the sensor stripes, electric current is unable to flow through the sensor.

Possible causes were weighted, and one of the fac-

tors influencing these defects might be the thermal expansion coefficients (CTE) mismatch between polymer and metal. When joining two materials, this property has to be taken into account during cooling processes, because it will induce tensile stress in one material and compressive stress in the other [23].

Measures were taken towards mitigating this issue, including promoting a slow cooling of the sample after the photoresist bake at 85 °C; in the development, the baking step at 110 °C was also adapted to 85 °C. Adopting these changes, the sample mask was modified to include 5 sensors with different sizes.

There's also an important aspect to consider: this micro-cracking phenomena was only observed in the films deposited on the thinnest polyimide (25 μm). The Stoney formula [24] presents a good explanation for this, which is the fact that the radius of curvature of substrate plus film increases with the square of the substrate thickness. This means that, considering the same amount of stress generated during deposition, the samples with PI-125 μm and PEN-75 μm have a larger radius of curvature, implying less bending of the sample. Upon heating, for example in the baking steps, the thermal stress will contribute to increase the residual stress of the substrate, thus decreasing the radius of curvature and causing the thin film to crack.

$$R_{s+f} = \frac{1}{6} \frac{E_s t_s^2}{\sigma_s t_f (1 - \nu)} \quad (8)$$

where R is the radius of curvature of the substrate and thin film structure, σ_s , E_s , t_s are the stress, Young's Modulus and the thickness of the substrate and t_f is the thickness of the film.

6. Device characterization: results and discussion

The samples in this work were designed to be directly connected to a printed circuit board (PCB) for structures characterization. Since the main scope of this analysis was to measure bent samples, an alternative solution to the conventional micro-probes had to be developed. Magnetic characterization at INESC-MN is performed on a setup

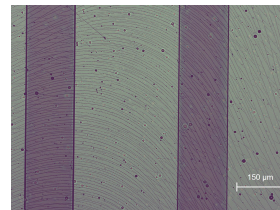


Figure 7: First sample fabricated, with cracks visible after the first layer lithography.

(Fig.8) comprising a Keithley 220 programmable current source, a Keithley 182 digital voltmeter, microscope, 4 micro-probes, and two coils capable of generating a field up to 140 Oe (14 mT).

Instead of the probes, samples are inserted in a flex cable connector (Fig.9c), which in turn was soldered to a PCB designed especially for this work (Fig.9b). In Fig.9a there is an example of a sample connected to the PCB and bent on one of the bending supports. These were 3D printed with different radii of curvature, namely 2.5, 10 and 12 mm.

It is important to highlight that the design of the samples mask was elaborated in accordance with this flex cable connector, which has 10 pads, so each sample has 5 sensors (each has 2 metal leads that fit exactly on top of the connector pads). The PCB was then designed to have also 10 leads and each pair of pins is connected to one sensor.

To integrate this assembly on the existing setup, the PCB is inserted in a ZIF (zero insertion force) connector attached to a terminal box (Fig.9d). This is shown in Fig.10, where a sample is mounted on the smallest bending support (2.5 mm radius); the setup is placed between the two coils for characterization. The connections between sensor and acquisition system are made through the terminal box with cables. This system also helps to prevent the sensors from cracking, as it allows to choose the sensor to measure on the terminal box without actually touching the sample. This is key when working with flexible substrates, as handling of the sample may lead to a decrease in performance of the sensors.

7. Anisotropic Magnetoresistance curves

The most important tool for characterizing the behavior and performance of a magnetoresistive sensor is a magneto-transport curve. The relevant parameters are the minimum and maximum resistance (R_{\min} and R_{\max}), which define the AMR ratio, as well as the saturation field. These curves have a bell shape, as discussed in Chapter 2, and display the resistance or AMR ratio as a function of the applied magnetic field.

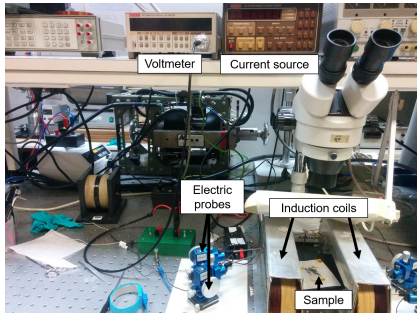


Figure 8: Measurement 140 Oe setup installed at INESC-MN.

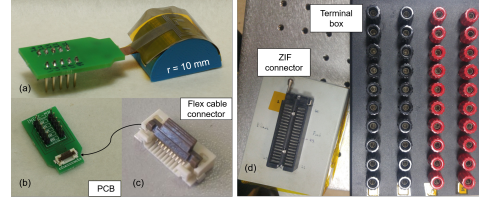


Figure 9: Components of the bending characterization setup: (a) Sample bent and inserted on the PCB connector; (b) PCB; (c) Flex cable connector; (d) ZIF connector and terminal box.

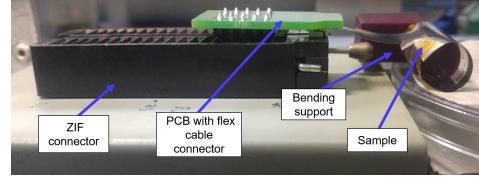


Figure 10: PCB inserted in the ZIF connector, with a sample mounted in a bent mode ready for measurements.

To obtain these curves, a sample is placed between the induction coils, which in turn generate a variable magnetic field. Measures were performed from - 14 to 14 mT, with a current bias of 1 μ A. Field steps were not constant throughout the whole measurement: from -14 to -4 the step was 2 mT, from -4 to 4 it was 0.4 mT (in order to increase resolution and linearity in this zone) and increases to 2 mT again until 14 mT. H_{sat} refers to the field at which the magnetization is saturated along the external applied field. Fig.11 shows a layout of the characterization, where H_{app} is the applied field, M and M' are the initial magnetization direction and the magnetization rotation with the field.

Measurements were performed in sequence as illustrated in Fig.12. As each sample has 5 sensors, all of them were first tested for output signal, and then to obtain a transport curve. The curves that

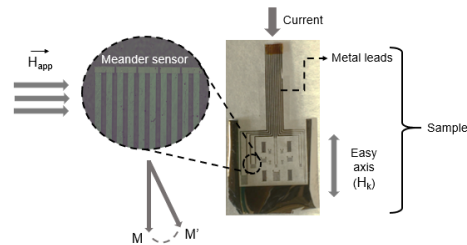


Figure 11: Characterization layout: H_{app} is the applied field, M and M' are the initial magnetization direction and the magnetization rotation with the field. The image shows a sample with a sensor close-up.

depicted the best electrical signal and shape were chosen.



Figure 12: Measurements sequence flowchart.

7.1. Ni₈₀Fe₂₀ curves

Ni₈₀Fe₂₀ was measured on the three substrates. The sample on PI-125 μm was not measured with $r_{\text{bend}} = 2.5$ mm due to handling difficulties caused by the stiffness of the substrate. Regarding the AMR signal, the typical values for films on silicon substrates go up to 2% [25], and on flexible substrates studies report that this value is around 0.6 to 1% [26].

Starting by comparing the curves without any bending (Fig.13 and first plot in all samples), there is a clear evidence that PI-125 μm is the substrate that yielded the highest AMR ratio, with values around 0.90%, very close to values obtained in silicon. Looking at the measured resistance, we can see that the values are around 4000 Ω for the three substrates, and since the measured sensors have different sizes, they also had different nominal resistances. The sensor on PI-125 μm showed the smallest resistance increase comparing to the nominal value, which indicates that it did not deteriorate during fabrication as much as the sensors on other substrates, presenting less defects such as micro-cracking. Regarding the saturation field, PI-25 μm presents the smallest value (1.6 mT), followed by PEN (2.2 mT) and PI-125 μm (2.3 mT).

Regarding Co₉₀Fe₁₀ samples, it was not possible to measure this film on PEN, nor with $r_{\text{bend}} = 2.5$ mm. The curves on PI-25 μm present a large amount of noise, and a very low AMR ratio. Literature reports AMR signals for CoFe alloys around 0.5 to 0.55% [27]. The presented values for H_{sat} are a rough estimate, as the curves shape does not allow

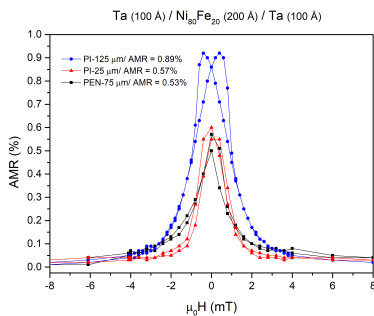


Figure 13: Ta 100 Å / Ni₈₀Fe₂₀ 200 Å / Ta 100 Å // on the three substrates AMR curves measured on flat mode ($r = \infty$).

a very precise estimation, but looking at the curves, this value seems to be constant with increased bending. Furthermore, they are significantly higher than the saturation values of Ni₈₀Fe₂₀, as expected. On PI-125 μm, the first two curves without bending refer to 2 different sensors; the first is a test sensor, meaning that it was measured with the micro-probes instead of the flex cable connector, while the second curve is the S4B sensor. Although their shape is very similar, S4B showed a considerable increase in resistance, as compared to the testing counterpart. This is probably due to degradation of the conductive metal leads, which in turn led to a loss of AMR signal. The curve with $r_{\text{bend}} = 10$ mm shows a further reduction of this output and increase in resistance. Also, this curve did not reach saturation even at 14 mT.

7.2. Anisotropy contributions and influence on sensor behavior

As discussed previously, there are different sources of anisotropy that influence the system. As stated earlier, H_{sat} is the field required to saturate the magnetization according to the applied magnetic field, and in order for this to happen, this field has to overcome the total anisotropy of the system, which makes magnetization lie along a certain direction.

When the thin film is patterned, shape anisotropy is no longer negligible and the demagnetizing field is an important factor that can be estimated to understand its influence on the total anisotropy.

The smaller the sensor width and the bigger the magnetization value, the more pronounced this phenomenon is. In the case of this work, the demagnetizing field contributes to anisotropy, but it is not the dominant factor, since it varies from 0.3 to 0.5 mT through all the samples, but the minimum saturation field measured is 1.6 mT.

Induced stress through bending is a crucial aspect to be considered. This parameter can be calculated through an equation deriving from the isotropic Hooke's law (Eq. 9):

$$\sigma_u = E_f \left(\frac{t_f + t_s}{2R} \right) \frac{1 + 2\frac{t_f}{t_s} + \frac{E_f t_f^2}{E_s t_s^2}}{\left(1 + \frac{t_f}{t_s}\right) \left(1 + \frac{E_f t_f}{E_s t_s}\right)} \quad (9)$$

where E_f , E_s are respectively the film and substrate Young's modulus, t_f , t_s are respectively the film and substrate thicknesses and R is the radius of curvature at which the sample is bent [28].

Finally, the field associated with the induced stress is calculated according to Eq. 10:

$$H_\sigma = \frac{2K_{u\sigma}}{\mu_0 M_s} \quad (10)$$

In $\text{Ni}_{80}\text{Fe}_{20}$ samples on PEN and PI-125 μm , H_σ has a strong contribution to the saturation field, as these values are in the same order of magnitude and are considerably larger than H_{dem} . The same does not hold for PI-25 μm , where both anisotropies contribute almost equally on both ferromagnetic alloys.

$\text{Co}_{90}\text{Fe}_{10}$ results are somewhat different, as seen that its saturation field on both substrates has a greater discrepancy from H_{dem} and H_σ . On PI-125 μm it was not possible to estimate H_{sat} because with the field of 14 mT the saturation of magnetization was not reached, meaning that $H_\sigma = 3.7$ mT is a very small contribution. This is probably due to the magnetocrystalline anisotropy of $\text{Co}_{90}\text{Fe}_{10}$ being more determining in the total anisotropy when compared to $\text{Ni}_{80}\text{Fe}_{20}$.

8. Conclusions

This dissertation focused on the fabrication and characterization of magnetic sensors based on anisotropic magnetoresistance onto three flexible substrates. Two different alloys ($\text{Ni}_{80}\text{Fe}_{20}$ and $\text{Co}_{90}\text{Fe}_{10}$) were deposited with different technologies and its quality was tested with different methods.

Resistivity measurements displayed consistent values with literature and previous works done at INESC-MN. X-ray diffraction analysis of PEN and $\text{Ni}_{80}\text{Fe}_{20}$ revealed highly textured materials with a single highly preferred crystallographic orientation, respectively and using Miller indices notation, (-110) and (111), which correspond to average interplanar distances of 3.40 Å and 2.03 Å.

A study of magnetic properties of as-deposited films was also performed. The results obtained for both properties are consistent with literature and among samples of the same alloy in different substrates. As expected, $\text{Co}_{90}\text{Fe}_{10}$ has higher coercive and anisotropy fields than $\text{Ni}_{80}\text{Fe}_{20}$, and therefore the estimated anisotropy constant is also higher for this material.

To characterize the fabricated sensors, a setup was developed and adapted to the existing magneto-transport characterization apparatus. Instead of the common electric micro-probes, samples are inserted in a flex cable connector soldered onto a PCB that allows the electric connection between sample and acquisition system.

AMR curves were obtained for each material deposited on different substrates and bending conditions. The tested curvature radii were $r_{bend} = 12, 10$ and 2.5 mm. The highest AMR ratio obtained was 0.90% in $\text{Ni}_{80}\text{Fe}_{20}$ // PI-125 μm sample, which is very close to values obtained on silicon counterparts. In general, both AMR signal and H_{sat} values seemed to be stable even with increased curvature. Only on PI-25 μm a reduction in signal is observ-

able with $r_{bend} = 2.5$ mm. $\text{Co}_{90}\text{Fe}_{10}$ curves yielded lower AMR ratios in general, the larger being 0.58% on PI-125 μm . Furthermore, the sample on PI-25 μm showed a strong presence of noise affecting the curves shape, so the estimated values of H_{sat} and H_{sw} are not as reliable as the ones for $\text{Ni}_{80}\text{Fe}_{20}$. This material exhibits a larger degradation in performance with increasing bending, as sample on PI-125 μm did not even reach saturation with the maximum magnetic field.

The demagnetizing field is not the dominant contribution for anisotropy in the measured sensors, but if we want to achieve smaller structures with only a few micrometers wide, special attention will be required to minimize this term. Induced stress through bending depicts a strong variation with substrate thickness, as for $\text{Ni}_{80}\text{Fe}_{20}$ // PI-25 μm , $\sigma_{2.5mm} = 216$ MPa and for PEN-75 μm , $\sigma_{2.5mm} = 1490$ MPa, which is substantially higher. This stress can be translated to an anisotropy constant, that also counts with the magnetostriction coefficient of the material and further analyzed as the stress induced field. It is recognizable that for $\text{Ni}_{80}\text{Fe}_{20}$ samples the stress anisotropy plays an important role on the saturation field, since both H_{sat} and H_σ are in the same order of magnitude. On the other hand, $\text{Co}_{90}\text{Fe}_{10}$ saturation field clearly has other strong contribution besides induced stress, which probably comes from the magnetocrystalline term, as it is perceptible through the H_k value that comes from the hysteresis curve.

In conclusion, although PI-125 μm seems to be a better substrate for the sensor layer, as it yielded better AMR signal, it has the drawback of not reaching the same curvature as easily as PEN-75 μm and PI-25 μm . The thinner polyimide showed the lowest AMR ratio, but on the other hand it also presented the lowest saturation field and stress values, with the advantage of conforming to almost any shape. For future work, further optimization of the fabrication techniques should be performed, namely on lithography steps to improve the sensor quality and minimize alignment errors. Successful fabrication of smaller sensors of, for example, 20 μm wide should be attained in order to characterize those structures and understand if it such sizes are a viable option. Furthermore, fabrication on PEN should be further explored with smaller foil thickness to improve conformability and reduce stress on the film. PI-25 μm seems to be a very promising material for flexible applications for the reasons stated earlier, so other bending radii should be used to study in depth the potential of this polymer.

References

- [1] B. Dieny, V. S. Speriosu, S. S. P. Parkin, B. A. Gurney, D. R. Wilhoit, and D. Mauri. Giant magnetoresistive in soft ferromagnetic multilayers. *Physical Review B*,

- 43(1):1297–1300, jan 1991. doi: 10.1103/physrevb.43.1297.
- [2] F. P. P. F. R. C. S. C. F. Magnetoresistive Sensors. *Journal of Physics: Condensed Matter*, 2007.
- [3] C. Zheng, K. Zhu, S. C. de Freitas, J.-Y. Chang, J. E. Davies, P. Eames, P. P. Freitas, O. Kazakova, C. Kim, C.-W. Leung, S.-H. Liou, A. Ognev, S. N. Piramanayagam, P. Ripka, A. Samardak, K.-H. Shin, S.-Y. Tong, M.-J. Tung, S. X. Wang, S. Xue, X. Yin, and P. W. T. Pong. Magnetoresistive Sensor Development Roadmap (Non-Recording Applications). *IEEE Transactions on Magnetics*, 55(4):1–30, apr 2019. doi: 10.1109/tmag.2019.2896036.
- [4] M. Melzer, M. Kaltenbrunner, D. Makarov, D. Kar-naushenko, D. Kar-naushenko, T. Sekitani, T. Someya, and O. G. Schmidt. Imperceptible magnetoelectronics. *Nature Communications*, 6(1), jan 2015. doi: 10.1038/ncomms7080.
- [5] Z. Wang, X. Wang, M. Li, Y. Gao, Z. Hu, T. Nan, X. Liang, H. Chen, J. Yang, S. Cash, and N.-X. Sun. Highly Sensitive Flexible Magnetic Sensor Based on Anisotropic Magnetoresistance Effect. *Advanced Materials*, 28(42):9370–9377, sep 2016. doi: 10.1002/adma.201602910.
- [6] J. M. D. Coey. *Magnetism and Magnetic Materials*. Cambridge University Press, 2009. doi: 10.1017/cbo9780511845000.
- [7] R. Slatter. Magnetoresistive (MR) Sensors for Angle-, Path- and Current Measurement in Harsh Environments. ., 2015. doi: 10.5162/SENSOR2015/B3.1.
- [8] A. N. V. da Silva. *Towards sub-100nm Magnetoresistive Devices: From Simulations to Applications*. PhD thesis, Instituto Superior Técnico, 2016.
- [9] T. McGuire and R. Potter. Anisotropic magnetoresistance in ferromagnetic 3d alloys. *IEEE Transactions on Magnetics*, 11(4):1018–1038, jul 1975. doi: 10.1109/tmag.1975.1058782.
- [10] V. Gehanno, P. Freitas, A. Veloso, J. Ferrira, B. Almeida, J. Soasa, A. Kling, J. Soares, and M. da Silva. Ion beam deposition of Mn-Ir spin valves. *IEEE Transactions on Magnetics*, 35(5):4361–4367, 1999. doi: 10.1109/20.799086.
- [11] P. Ripka. *Magnetic Sensors: Principles and Applications*. Elsevier, 2007.
- [12] T.-R. Ger, H.-T. Huang, C.-Y. Huang, and M.-F. Lai. Single cell detection using 3D magnetic rolled-up structures. *Lab on a Chip*, 13(21):4225, 2013. doi: 10.1039/c3lc50721a.
- [13] L. Jogschies, D. Klaas, R. Kruppe, J. Rittinger, P. Taptimthong, A. Wienecke, L. Rissing, and M. Wurz. Recent Developments of Magnetoresistive Sensors for Industrial Applications. *Sensors*, 15(11):28665–28689, nov 2015. doi: 10.3390/s151128665.
- [14] J.-H. Kwon, W.-Y. Kwak, and B. K. Cho. Magnetization Manipulation of a Flexible Magnetic Sensor by Controlled Stress Application. *Scientific Reports*, 8(1), oct 2018. doi: 10.1038/s41598-018-34036-z.
- [15] A. Guittoum, A. Bourzami, A. Layadi, and G. Schmerber. Structural, electrical and magnetic properties of evaporated permalloy thin films: effect of substrate and thickness. *The European Physical Journal Applied Physics*, 58(2):20301, may 2012. doi: 10.1051/epjap/2012110343.
- [16] Y.-T. Chen, S. H. Lin, and Y. C. Lin. Effect of Low-Frequency Alternative-Current Magnetic Susceptibility in Ni80Fe20Thin Films. *Journal of Nanomaterials*, 2012:1–6, 2012. doi: 10.1155/2012/186138.
- [17] S. Sheng, W. Li, M. Li, and G. Yu. Investigation on interface of NiFeCr/NiFe/Ta films with high magnetic field sensitivity. *Rare Metals*, 31(1):22–26, jan 2012. doi: 10.1007/s12598-012-0455-1.
- [18] S. Cakmaktepeand and S. Diken. Magnetic and structural analysis of sputtered Co90Fe10/Au multilayer films for magnetic recording applications. *Journal of Optoelectronics and Advanced Materials*, 18, p107-111, 2016.
- [19] Y. K. Kim. Soft magnetic properties of sub 10 nm NiFe and Co films encapsulated with Ta or Cu. *physica status solidi (a)*, 201(8):1859–1861, jun 2004. doi: 10.1002/pssa.200304601.
- [20] R. Bonin, M. L. Schneider, T. J. Silva, and J. P. Nibarger. Dependence of magnetization dynamics on magnetostriction in NiFe alloys. *Journal of Applied Physics*, 98(12):123904, dec 2005. doi: 10.1063/1.2143121.
- [21] S. Merabtine, F. Zighem, A. Garcia-Sanchez, V. Gunasekaran, M. Belmeguenai, X. Zhou, P. Lupo, A. O. Adeyeye, and D. Faurie. Origin of relationship between ferromagnetic response and damage in stretched systems. *Scientific Reports*, 8(1), sep 2018. doi: 10.1038/s41598-018-32149-z.
- [22] J. Rittinger, P. Taptimthong, L. Jogschies, M. C. Wurz, and L. Rissing. Impact of different polyimide-based substrates on the soft magnetic properties of NiFe thin films. In J. L. Sánchez-Rojas and R. Brama, editors, *Smart Sensors, Actuators, and MEMS VII and Cyber Physical Systems*. SPIE, may 2015. doi: 10.1117/12.2178765.
- [23] A. International. Chapter 2: Thermal expansion. Technical report, The Materials Information Society, 2002.
- [24] Y. Y. Hu and W. M. Huang. Thermal Stress Analysis and Characterization of Thermomechanical Properties of Thin Films on an Elastic Substrate. In *Handbook of Manufacturing Engineering and Technology*, pages 1–71. Springer London, 2013. doi: 10.1007/978-1-4471-4976-7_51-1.
- [25] X. Tang, W. Du, J. Yu, H. Zhang, and H. Su. A flexible way to modulate the detection range of anisotropic magnetoresistance by exchange bias field. *Journal of Magnetism and Magnetic Materials*, 476:469–471, apr 2019. doi: 10.1016/j.jmmm.2019.01.012.
- [26] T. Griesbach, M. C. Wurz, and L. Rissing. Design, Fabrication, and Testing of a Modular Magnetic Field Microsensor on a Flexible Polymer Foil. *IEEE Transactions on Magnetics*, 48(11):3843–3846, nov 2012. doi: 10.1109/tmag.2012.2198798.
- [27] S. Srichandan. *Electrical and thermal transport coefficients of CoFe thin films deposited on a microcalorimeter*. PhD thesis, Universitat Regensburg, 2016.
- [28] M. Gueye, P. Lupo, F. Zighem, D. Faurie, M. Belmeguenai, and A. O. Adeyeye. Unambiguous magnetoelastic effect on residual anisotropy in thin films deposited on flexible substrates. *EPL (Europhysics Letters)*, 114(1):17003, apr 2016. doi: 10.1209/0295-5075/114/17003.